Relationships between Structure and Rheology in Model Nanocomposites of Ethylene−Vinyl-Based Copolymers and Organoclays

Mikhail Y. Gelfer,[†] Christian Burger,[†] Benjamin Chu,[†] Benjamin S. Hsiao,*[,†] Aleksey D. Drozdov,[‡] Mayo Si,[§] Miriam Rafailovich,[§] Bryan B. Sauer,[⊥] and Jeffrey W. Gilman[#]

Chemistry Department, State University of New York, Stony Brook, New York 11794-3400; Chemical Engineering Department, West Virginia University, Morgantown, West Virginia 26506; Materials Science and Engineering Department, State University of New York, Stony Brook, New York 11794; Central Research and Development, DuPont Company, Wilmington, Delaware 19880; and Fire Research Division, National Institute of Standards and Technology, Gaithersburg, Maryland 20899-8665

Received December 2, 2004; Revised Manuscript Received February 11, 2005

ABSTRACT: A series of nanocomposites prepared by melt-blending of Cloisite organoclays with ethylene-*co*-vinyl acetate (EVA) and ethylene-*co*-methyl acrylate (EMA) copolymers were investigated by using small-angle X-ray scattering (SAXS), wide-angle X-ray diffraction (WAXD), transmission electron microscopy (TEM), thermogravimetric analysis (TGA), and rheological techniques. SAXS and TEM results confirmed mixed clay intercalation and exfoliation in all tested nanocomposites. The melting temperature, T_m, and crystalline structure (orthorhombic) in EMA and EVA were not significantly affected by the presence of organoclays, indicating that the clay particles were predominantly confined to the amorphous phase. Rheological properties above T_m were very similar in EVA and EMA nanocomposites. Both systems exhibited pseudo-solid rheological behavior in small-strain oscillatory shear experiments, yet they could yield and flow under a steady shear, which is characteristic of physical gelation. The pseudo-solid rheological behavior in EVA and EMA nanocomposites becomes more pronounced at higher contents of organoclay and at higher temperatures. SAXS results indicated that the silicate gallery spacings (d), intercalated by EVA and EMA chains, decreased with increasing temperature. This can be attributed to the reduced compatibility between organoclay and polymer (i.e., a LCST-type phase behavior). The unusual rheological properties of the nanocomposites at high temperatures were probably due to the formation of a 3D network of clay tactoids. Novel analytic models were proposed to describe rheological data from meltlike to gellike behaviors in EVA− and EMA−organoclay nanocomposites.

Introduction

Polymer nanocomposites containing surfactant-modified layered silicates (organoclays) have attracted a great deal of research interest in recent years. It has been demonstrated that the incorporation of organoclays could result in drastic changes in the morphology, mechanical, and rheological properties.[1−7] Some recent rheological studies[3,7] of polymer−organoclay nanocomposites indicated that the dispersed organoclay particulates might act as physical cross-linkers, resulting in a solidlike rheological behavior at temperatures far above the glass transition temperature (T_g) or melting temperature (T_m). This behavior has been attributed to the end-tethering of polymer chains on the mineral surfaces and the formation of a physical network by clay aggregates and/or individual platelets.[3,5] However, there are still many unresolved questions concerning the relationships among the molecular structure of polymer chains and the structures of minerals and surfactants in organoclays as well as the morphology, thermal behavior, and rheological properties of nanocomposites, which forms the basis of this study.

In this work, we have investigated the particular relationship among the molecular structure of polymer chains, morphology, and rheology of nanocomposites prepared by melt-blending of Cloisite organoclays and ethylene-*co*-vinyl acetate (EVA) and ethylene-*co*-methyl acrylate (EMA) random copolymers. These materials were chosen as model nanocomposites for the following reasons. In our previous publications,[7,8] we described the unusual thermorheological behavior of EVA−organoclay nanocomposites at high temperatures. These materials exhibited a pseudo-solid rheological behavior, which became more pronounced upon heating, especially at temperatures above 180−200 °C. At lower temperatures as well as at lower organoclay content ($\phi \leq 2$ wt %), the EVA nanocomposites predominantly recovered back to meltlike rheology. The dielectric spectroscopic study[8] indicated that the presence of organoclays only had a weak influence on the local segmental mobility of the EVA chains. Thus, EVA− and EMA−organoclay nanocomposites, which exhibited a different degree of intercalation/exfoliation, could be considered as good model systems for the study. The gellike behavior of the EVA− and EMA−organoclay nanocomposites, resulting from the formation of a three-dimensional (3D) network of clay tactoids, can be probed simultaneously by small-oscillatory rheological experiments as well as small-angle X-ray scattering (SAXS) study.

To quantitatively describe the rheological behavior from meltlike to gellike for nanocomposite melts, we have developed novel data analysis schemes in this

[†] Chemistry Department, SUNY.
[‡] West Virginia University.
[§] Materials Science and Engineering Department, SUNY.
[⊥] DuPont Company.
[#] National Institute of Standards and Technology.
* To whom correspondence should be addressed: e-mail bhsiao@notes.cc.sunysb.edu, Tel 631-632-7793, Fax 631-632-6518.

10.1021/ma0475075 CCC: $30.25 © 2005 American Chemical Society
Published on Web 04/09/2005

study. In addition, we have attempted to correlate the unique rheological behavior to the clay microstructures. To be specific, we observed the evidence of phase segregation between organoclay and EVA or EMA matrix at higher temperatures, which exhibited a low critical solution temperature (LCST) type phase behavior. The rheological behavior of the nanocomposites below and above gel transition was investigated over a wide temperature range (110−260 °C), and the corresponding $G'(\omega)$ and $G''(\omega)$ data were quantitatively fit by two analytic models. It was found that the rheology of pure EVA and EMA melts and of nanocomposites below the gelation threshold could be described by the modified Cole (MC) model,[9] while the rheology of EVA−clay and EMA−clay gels could be described by the log−normal (LN) distributions of relaxation times. The corresponding morphologies of polymer nanocomposites were followed by temperature-resolved SAXS and wide-angle X-ray diffraction (WAXD) techniques, where the SAXS data were interpreted using a novel analytic technique[10] to extract the temperature dependence of structure parameters. The temperature dependencies of parameters in the rheological models were correlated with the composition and the morphology of the polymer matrix as well as the organoclay content in nanocomposites.

Experimental Section

Samples and Preparation. Ethylene-*co*-vinyl acetate (EVA) and ethylene-*co*-methyl acrylate (EMA) copolymer samples were received from DuPont Co. The content of vinyl acetate units in EVA10 was 10.75 mol %, EVA8 was 8.15 mol %, and EVA3 was 3.1 mol %. The values of melt index (g/10 min) for EVA 10 was 43.0, EVA8 was 19.0, and EVA3 was 0.8, indicating that the weight-average molecular weights (M_w) of the samples were in the following order: EVA3 > EVA8 > EVA10. The content of methyl acrylate comonomer in EMA3 samples was 3.1 mol %. The value of the melt index for EMA3 was 2, and the corresponding molecular weights of EMA3 were $M_n \approx 20\,000$ g/mol and $M_w \approx 70\,000$ g/mol. Both EVA and EMA copolymers were structurally similar to low-density polyethylene (LDPE), i.e., contain a significant amount of long-chain branches.

Organoclays used in this study included Cloisite 6A (C6A) and Cloisite 20A (C20A), manufactured by the Southern Clay Co. Based on the data provided by Southern Clay, all organoclays contain the same mineral base (montmorillonite clay, Wyoming Cloisite) and identical surfactant, dimethyl dihydrogenated talloammonium chloride (DMDTA). The content of the surfactant in organoclays varied from 45 wt % (C6A) to 35 wt % (C20A). DMDTA was a blend of surfactants prepared from natural products by Akzo Nobel. According to Akzo Nobel, the major component in this blend was dimethyl dioctadecylammonia chloride (DMDOA); minor components included (in the order of decreasing content) dimethyl octadecylhexadecylammonia chloride, dimethyldihexadecylammonia chloride, and a small (<3 wt %) amount of tertiary ammonia chlorides (such as dimethyloctadecylammonia chloride and dimethylhexadecylammonia chloride).

All polymer−organoclay nanocomposites were prepared by melt-blending of EVA (or EMA) with organoclays at 150 °C under the flow of nitrogen using a Brabender melt-mixer. The clay contents (ϕ) in the nanocomposites were varied from 2 to 10 wt %. All components were used as received from the manufacturers.

Characterization Techniques. Thermogravimetric analysis (TGA) measurements were performed using TGA 2950 (TA Instruments). Parallel measurements were done in both nitrogen and air environments in order to evaluate the effect of oxidative degradation on the overall weight loss of organoclays. TGA measurements were carried out using a heating rate of 10°C/min from 30 to 900 °C. Two thermal protocols were applied: (1) heating at a constant rate of 10 °C/min from 30 to 900 °C, (2) multiple staged temperature profiles, identical to those used in SAXS measurements. The chosen multiple staged temperature profiles were as follows. The sample was first held isothermally for 3 min. Multiple heating steps were taken from 30 to 260 °C at every 20 °C interval. The heating rate between each step was 30 °C/min, and the holding time during the isothermal step was 3 min. Upon reaching 260 °C and being held for 3 min, three cooling steps were also carried out at 200, 160, and 80 °C, respectively. The cooling rate between each step was also 30 °C/min.

Simultaneous SAXS and WAXD measurements were performed at the X27C Beamline in the National Synchrotron Light Source (NSLS), Brookhaven National Laboratory. The wavelength of the X-ray was 1.366 Å. The collimation was carried out by three-pinhole geometry. A dual-chamber temperature jump apparatus was used, which held the experimental temperature with accuracy around ±1 °C. Two 1-D wire detectors (European Molecular Biology Laboratory, Grenoble, France) were used for simultaneous SAXS/WAXD detection. The sample-to-detector distances for SAXS were 840 mm and for WAXD was 130 mm. The scattering angle in SAXS was calibrated by a silver behenate standard, and the diffraction angle in WAXD was calibrated by an Al_2O_3 standard from the National Institute of Standards and Technology. All signals were corrected for beam fluctuations and sample absorptions. Similar multiple-stage temperature profiles, as employed in the TGA study, were also used for in-situ SAXS/WAXD measurements.

Small strain oscillatory shear and shear rate sweep rheological measurements were carried out using RMS 605 strain-controlled rheometer, manufactured by Rheometrics Scientific (Piscataway, NJ). A 25 mm parallel plate fixture was used, and a constant strain amplitude ($\gamma = 0.06$) was employed in all dynamic measurements. The frequency scan ($0.1 < \omega < 100$ rad/s) for the acquisition of oscillatory shear data was repeated four times at each experimental temperature. It was shown that, for all tested samples, the isothermal rheological properties (storage and loss moduli $G'(\omega)$ and $G''(\omega)$) remain stable on the time scale of 1800 s. To avoid the degradation of polymer substrates, all rheological measurements were performed under the flow of nitrogen.

Transmission electron microscopy (TEM) measurements were carried out on a JEOL 2000FX TEM instrument operated at 160 kV acceleration voltage. Samples were cryo-microtomed at −150 °C using an ultramicrotome (Leica Ultracut UCT) equipped with diamond knife and water flotation bath to obtain sections of 70 nm thickness thin films for TEM imaging.

Data Analysis for SAXS and Rheological Data. SAXS results from nanocomposites were analyzed in the framework of the modified Hermans model.[10,11] The detailed analytical schemes for organoclays and corresponding nanocomposites have been described by us elsewhere;[10] they will not be repeated here.

For the analysis of unique rheological properties (i.e., typical meltlike behavior at low temperatures, gelation behavior at high temperatures) in EMA− and EVA−organoclay nanocomposites,[7−9] a new analytical scheme was developed for this study. Such an approach is currently not available in the field; it is outlined as follows. The complex modulus G^* can be expressed as a linear superposition of idealized Maxwell components in the form of a distribution (H) of relaxation times (τ)

$$G^*(\omega) = G_{ind} + i\omega G \int_0^\infty H(\tau)(1 + i\omega\tau)^{-1}\,d\tau \equiv G_0 + Gg(\omega) \quad (1)$$

where G is the scaling factor, G_{ind} is the frequency-independent modulus (can be a complex), which may be used to describe the state of gelation in physically or chemically cross-linked materials, G_0 is the real part of the frequency-independent modulus, and $g(\omega)$ represents the frequency-dependent modulus.

The relaxation time distribution of a single Maxwell element can be given by Dirac's δ-function

$$H(\tau) = \tau_0\delta(\tau - \tau_0), \quad g(\omega) = i\omega\tau_0(1 + i\omega\tau_0)^{-1} \tag{2}$$

As a probability density distribution, $H(\tau)$ is positive everywhere and can be normalized to unity integral. It can be kept continuous as in eq 1 or be approximated as a discrete sum of δ-functions, linearly transforming to a corresponding discrete sum for the complex modulus:

$$H(\tau) = \sum_{n=1}^{N} c_n\tau_n\delta(\tau - \tau_n), \quad g(\omega) = i\omega\sum_{n=1}^{N} c_n\tau_n(1 + i\omega\tau_n)^{-1} \tag{3}$$

where the normalization condition must be fulfilled by the coefficients c_n. The discrete decomposition in eq 3 has been the basis for many numerical approaches, such as Winter's parsimonious model,[12] which was primarily concerned with the problem of "illposedness" and how to overcome it.

An alternative approach can be derived by choosing empirical functions in simple analytically closed form to parametrize the experimental data. Such a technique had been employed in some very early studies of relaxation phenomena, including the work by Kohlrausch[13] to deal with mechanical relaxation in the time domain, as well as those by Davidson and Cole[14] and Havriliak and Negami[15] to deal with dielectric relaxation (complex compliance) in the frequency domain. On the basis of the approach for mechanical relaxation (complex modulus), we have adopted the following function to express the $g(\omega)$ function:

$$g(\omega) = (i\omega\tau_0)^{\alpha}[1 + (i\omega\tau_0)^{\alpha}]^{-\beta} \tag{4}$$

where α and β represent the parameters describing the shape of the distribution of relaxation times $H(\tau)$ and τ_0 is proportionate to the center of the distribution. Some of the shape parameters can be fixed as unity to simplify the model (e.g., $\beta = 1$ for the Cole–Cole function[9] and $\alpha = 1$ for the Davidson–Cole function[14]). The parameters α and β are usually in the range between 0 and 1. Their effects can be thought of as the broadening of the ideal Maxwell functions in eq 1, both in the frequency and in the relaxation time domains. Note that in this case the problem of "illposedness" can be tackled by using the smaller number of parameters in combination with physically sound shapes and asymptotes of the functions. Thus, the additional regularization or other stabilization of the approach is not necessary, although it can still be easily implemented.

The use of empirical functions to model the complex compliance can be facilitated by the observation that every analytical function of this type can be inverted to its relaxation time distribution in a purely algebraic way, known as Stieltjes' inversion[16,17]

$$H(\tau) = \pi^{-1}\,\mathrm{Im}\,g(i/\tau) = \pi^{-1}\,\mathrm{Im}\,\frac{G^*(i/\tau) - G_0}{G} \tag{5}$$

We note that the imaginary part Im sometimes does not implement the needed difference along the branch cut in the Riemann plane, which must be exercised with care.[16,17] It is interesting to note that the Stieltjes inversion appears to work well even when the function $g(\omega)$ does not fulfill the necessary boundary conditions ($g(\omega)$ is the transform of a normalized probability density distribution based on eq 1). Applying the Stieltjes inversion to an arbitrary analytical function that fits the experimental data in a finite ω range, within certain limits, can result in a relaxation time distribution. This distribution provides a reasonable description for the τ range, corresponding reciprocally to the given ω range, and also agrees well with the output of the discrete numerical methods.

The asymptotic behavior for small and large values of the function in eq 4 and its transform in the relaxation time domain are given by relatively slow decaying algebraic power laws with small exponents, implying a certain qualitative nature of the relaxation time distribution, which may or may not be applicable. A qualitatively different distribution with a faster asymptotic decay is the log–normal distribution, which can be expressed as follows:

$$H_{\mathrm{LN}}(\tau) = (2\pi\sigma^2)^{-1/2}\exp[-\ln(\tau/\tau_0)^2/(2\sigma^2)] \tag{6}$$

where τ_0 and σ are parameters, whose physical significances have been described by Drozdov.[18,19]

It appears that, by using the log–normal distribution in its original form (eq 6), the complex modulus calculated by the integration in eq 1 cannot be solved in a closed analytical form. To overcome this problem, in the spirit of the central limit theorem, we can replace eq 6 with the following algebraic approximation

$$H(\lambda) = H_0 2^{-\lambda}\,\mathrm{sech}^{\lambda}[\ln(\tau/\tau_0)/2] = H_0(\tau/\tau_0)^{\lambda}/2(1 + \tau/\tau_0)^{-\lambda} \tag{7}$$

where λ and τ_0 are parameters, sech is the hyperbolic secant with $\mathrm{sech}(x) = 1/\cosh(x)$, the normalization constant $H_0 = \Gamma(\lambda)/\Gamma(\lambda/2)^2$, where Γ is the Gamma function, and the variance is $\sigma^2 = 2\psi'(\lambda/2)$ where ψ' is the derivative of the digamma function $\psi'(x) = \mathrm{d}^2[\ln\Gamma(x)]/\mathrm{d}x^2$. In the limit of infinitely large λ, the original log–normal distribution in eq 6 can be restored

$$\lim_{\lambda\to\infty} H_{\lambda}(\tau) = H_{\mathrm{LN}}(\tau) \tag{8}$$

For sufficiently large λ, eq 8 is a good approximation; for small λ values, eq 7 constitutes an empirical relaxation time distribution. The distribution in eq 7 can be crafted such that the integration in eq 1 can be performed in an analytically closed form.

$$g_{\lambda}(\omega) = \frac{i\omega\tau_0}{2}\,{}_2F_1(1,1 + \lambda/2;1 + \lambda;1 - i\omega\tau_0) \tag{9}$$

where ${}_2F_1(a,b;c;z)$ is the hypergeometric function that needs to be analytically continued for $|z| > 1$. For integer parameter λ, the hypergeometric function in eq 9 can be simplified to an elementary algebraic form, which also removes the issues of analytic continuation. For example, for $\lambda = 12$, which generates a distribution reasonably close to log–normal, we have

$$\begin{aligned} g_{12}(x) = [&12x - 165x^2 + 1100x^3 - 4950x^4 + 19800x^5 + \\ &4620x^6 - 27720x^7 + 9900x^8 - 3300x^9 + 825x^{10} - \\ &132x^{11} + 10x^{12} + 27720x^6\ln(x)]/[10(1 - x)^{12}] \end{aligned} \tag{10}$$

where $x = i\omega\tau_0$. The special cases for the other integer λ are readily available using standard symbolic software packages.

A problem of the distribution in eq 7 is that it ties the width of the distribution to its shape. For a sufficiently large parameter λ, i.e., sufficiently narrow distributions, this is of no concern since the shape of the distribution is already very close to log–normal and λ can be thought of as a parameter controlling its width. However, for smaller λ (i.e., broader distributions) this will not be the case and the shape of the distribution will change with its width. To overcome this problem and also to achieve the convenience of dealing only with simple algebraic functions, we can fix the parameter λ at a sufficiently large integer value, say $\lambda = 12$ and, in the spirit of the Cole-based functions in eq 4, introduce an additional parameter a (the relaxation time distribution shape parameter) to control its width

$$g(x) = g_{12}(x^a) \tag{11}$$

where $x = i\omega\tau_0$ as above. The exact relaxation time distribution H corresponding to eq 11 is, of course, readily available through the Stieltjes inversion in eq 5.

Results

Thermal Stability by TGA. TGA results show that in an inert atmosphere the presence of organoclay does

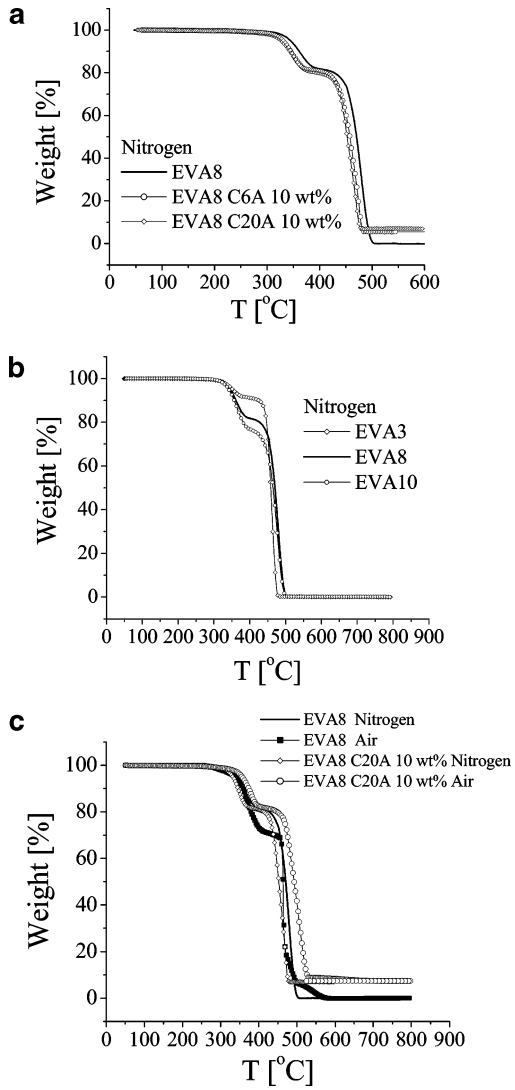

Figure 1. TGA thermograms of EVA nanocomposites to probe: (a) the effect of surfactant content in organoclay on the thermal stability of EVA−organoclay nanocomposites in nitrogen, (b) the effect of vinyl acetate (VA) content on the thermal stability of EVA, (c) the effect of atmosphere on stability of EVA−organoclay nanocomposites. A heating rate of 10 °C/min was used in all measurements.

not have an appreciable effect on the thermal stability of the EVA matrix (Figure 1a). The TGA curves for varying EVA polymers and corresponding nanocomposites can be divided into two regions for discussion: (1) below 280 °C and (2) above 280 °C. In pure EVA8, the weight loss below 250 °C is insignificant, while the weight loss in EVA8−organoclay (C29A and C6A) composites is noticeable but rather small (e.g., 0.5 wt % at 250 °C for EVA8−C20A vs 1 wt % for EVA8−C6A). The earlier onset of the weight loss in nanocomposites can be related to the desorption and/or thermal degradation of surfactant molecules in organoclays, which takes place at 180 °C.[20] It is not surprising that the weight loss below 280 °C is more pronounced in the system containing organoclays with higher surfactant content (i.e., C6A > C20A). Generally, below 280 °C, the TGA curves in air and nitrogen are quite similar.

The rapid weight loss starts at temperatures above 280 °C. It is seen that the rates of the weight loss for both EVA (Figure 1b) and its nanocomposites (Figure 1c) display two distinct maxima. The intensity of the first maximum is found to increase with the increase in the content of polar vinyl acetate (VA) monomer (Figure 1b). Thus, it is conceivable that the first maximum may correspond to the degradation of polar VA units and the neighboring CH_2 segments, while the second maximum may be due to the thermal degradation of longer polyethylene segments.

Under the nitrogen environment, the thermal stability of EVA is not strongly affected by the presence of organoclays. Weight loss below 280 °C is more pronounced in nanocomposites than in pure polymer, which can be attributed to the loss of surfactant component in organoclays. On the other hand, under the air environment, the onset of degradation in nanocomposite is shifted more than 50 °C toward the higher temperatures, as compared to pure EVA (Figure 1a,c). Higher thermal stability of nanocomposites in air (implying the reduced flammability) can be partially attributed to the lower gas permeability due to the presence of clay particulates. It is possible that the impermeable silicate barrier can slow down the oxygen diffusion, thus hindering the oxidation process. Another factor contributing to the lower flammability of nanocomposites is the formation of thermally stable silicate-rich chars, induced by the presence of mineral nanoparticles.[21] The charring processes, related to the oxidative dehydrogenation of the polymer matrix, may be catalyzed by dispersed aluminosilicate particles.[22]

In contrast to the ramping measurements in TGA, in stepwise experiments (Figure 2a,b), the weight loss in air is more pronounced than in nitrogen, which may be related to the oxidative degradation of the polymer matrix and the surfactant component in organoclays. Obviously, the charring process, which greatly slows down the weight loss in the temperature ramping measurements, is insignificant at relatively low temperatures (T < 260 °C) used in stepwise experiments. These results are consistent with the data previously observed in pure Cloisite organoclays.[10]

Crystalline Structure Changes and Melting Behavior by WAXD. Temperature-resolved WAXD profiles confirmed the same crystalline structure (orthorhombic) and the similar melting behavior as well as transition temperatures in pure EVA3 and EVA3−C20A (10 wt %) nanocomposites (Figure 3a,b). These observations are in good agreement with the differential scanning calorimetry (DSC) data previously reported.[7] On the basis of WAXD results and the DSC data,[7] we argue that the effect of organoclay on the crystalline phase in EVA is insignificant. It is known that in ethylene-based copolymers side chains (short branches) larger than the methyl group are excluded from the crystalline domain and aggregated into the amorphous phase.[23−25] Consequently, the amorphous domains in EVA or EMA are enriched by the polar VA or MA units. We hypothesize that the organoclay particulates dispersed in the EVA matrix have higher affinity to the polar VA units, so they are predominantly confined to the amorphous phase where the VA content is high. Thus, the influence of organoclays on the crystalline domain formed by nonpolar ethylene segments is minimal.

Clay Morphology in Nanocomposites by SAXS. Strong scattering peaks, related to the morphology of organoclay, can be distinctly observed by SAXS in EVA and EMA nanocomposites containing C6A. These observations suggest that the layered clay structures are partially preserved in the C6A-based systems. It is found that the SAXS maxima in nanocomposites are

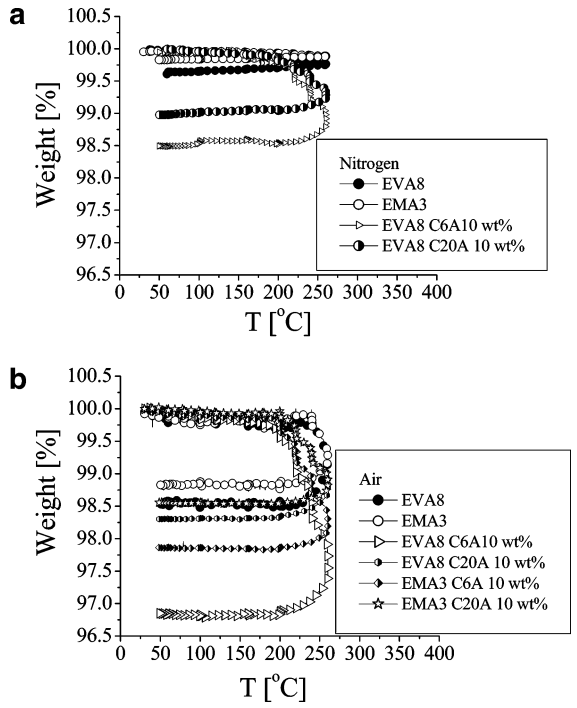

Figure 2. Effects of organoclay on the thermal stability of EVA−organoclay composites using the temperature steps protocol in TGA.

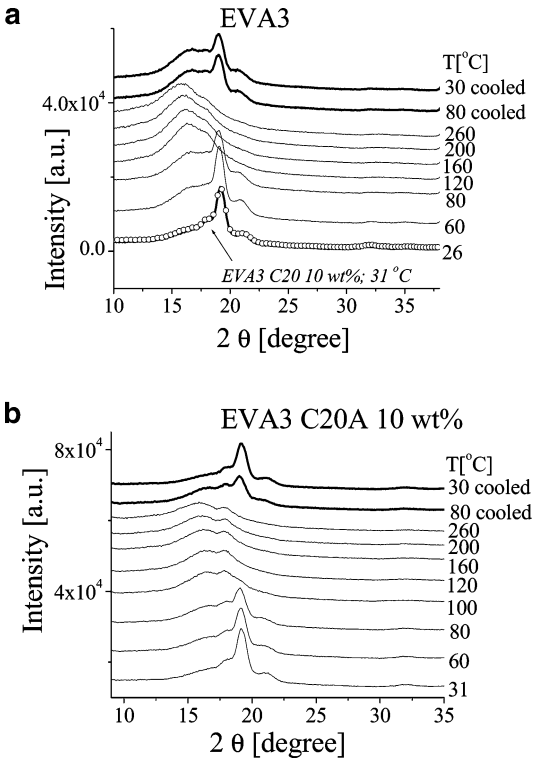

Figure 3. Effect of organoclay on the crystalline structure in (a) EVA3 at varying temperatures (the WAXD profile of EVA3C−20A (10 wt %) at 31 °C is also included for comparison) and (b) EVA3−C20A nanocomposite (the C20A content was 10 wt %) at varying temperatures.

shifted toward lower s values when compared to pure organoclays,[4,10] which is consistent with intercalation of organoclay structures by the EVA chains. The intercalation process implies good compatibility between polymer chains and organoclays, where in incompatible systems, the effect of polymer matrix causing the change in the d-spacing in dispersed organoclays is insignificant.

Parts a and b of Figure 4 illustrate SAXS profiles taken at varying temperatures for EVA8−C6A and EMA3−C6A nanocomposites, respectively, which allow for in-situ monitoring of the temperature dependence of nanocomposite morphology. It is known that the shape and the positions of scattering peaks in SAXS profiles for organoclays and polymer−clay nanocomposites are strongly affected by the characteristics of the layer thickness distribution.[10,26] Thus, in most cases, the average d-spacing (d_{av}) of the clay layer separation distance cannot be evaluated only from the position of the first scattering maximum at s_{max} ($s = 2\lambda^{-1} \sin \theta$, 2θ being the scattering angle and λ being the wavelength) using Bragg's law ($d_{av} = 1/s_{max}$). To ensure reliable results, the d_{av} values presented in this work were determined on the basis of a comprehensive analysis of SAXS traces using the algorithm proposed in our previous publication.[10]

It is interesting to see that the temperature dependence of d-spacings for both EVA− and EMA−C6A systems, as shown in Figure 4c, can be separated into three regions for further discussion. In the initial temperature range of 30−75 °C, the multiple scattering peaks are equidistant at the s scale (i.e., $s_2 = 2s_1$, where s_1 represents the position of the first-order peak and s_2 represents the position of the second-order peak), and the temperature dependence of d spacing is rather weak (Figure 4a,b). At temperatures in the range 75−200 °C, the d-spacing drastically decreases with the increase in temperature, but the scattering peaks remain equidistant at the s scale ($s_2 = 2s_1$). In the temperature range of 200−260 °C and during subsequent cooling, the scattering signals drastically broaden and become nonequidistant ($s_2 > 2s_1$, as shown in Figure 4a,b). Our previous results[10] showed that the average d-spacing in C6A organoclay, in the absence of polymer, changed from 3.6 to 3.3 nm as the temperature increased from 30 to 260 °C. The reduction of d-spacing in pure organoclay was more pronounced at higher temperatures, which could be attributed to the loss of surfactant due to thermal degradation. In contrast, the d-spacing in EVA-intercalated C6A (nanocomposites) was found to decrease from 4.1 to 3.5 nm, with most changes occurring at relatively low temperatures (75−180 °C). TGA results indicated that the loss of surfactant was insignificant in nanocomposites within this temperature range.

In Figure 4c, we suggest that changes in the SAXS profiles of the nanocomposites occurring above 200 °C can also be attributed to a thermal degradation of organoclays (i.e., debonding of surfactant molecules on the clay surface, resulting in the collapse of organoclays), which causes disordering in the remaining clay stacks.[10] The reasons for further broadening of scattering peaks during the cooling are not yet completely understood; however, we speculate that the rearrangement of EVA molecules can deintercalate and reintercalate the clay stacks during the heating and cooling cycle, respectively, which would result in the increased disorder in silicate stacks. It is interesting to note that the changes in SAXS profiles caused by degradation of organoclays during 30−260−30 °C heating−cooling cycles are far more pronounced in EVA− than in EMA− organoclay systems. These results are in a good agreement with the step-TGA data, showing far stronger weight loss in EVA than in EMA systems, containing

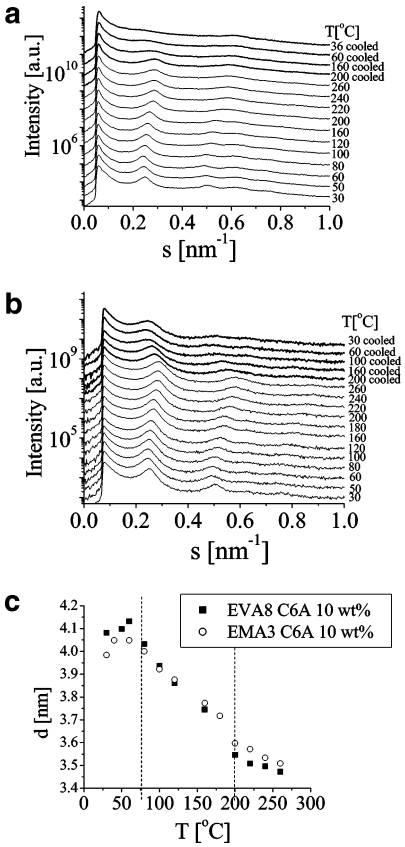

Figure 4. In-situ SAXS profiles of (a) EVA8−C6A and (b) EMA3−C6A nanocomposites containing 10 wt % of organoclay (sample was held for 3 min at each temperature; subscript "cld" represents the data acquired during cooling from 260 °C to room temperature). (c) Temperature dependence of d-spacing during the heating scan.

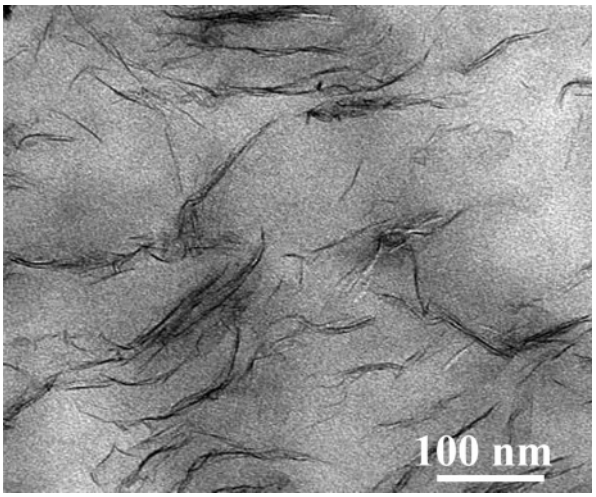

Figure 5. TEM micrograph of an EVA3−C20A (10 wt %) nanocomposite sample, where the intercalated clay stacks is found to coexist with individual platelets.

the identical amount of organoclay (Figure 2). The exact reason causing the observed difference in thermal stability of organoclays dispersed in structurally similar materials is not yet completely understood. We speculate that the diffusion rate of the free surfactant molecules through EMA nanocomposite at high temperatures may be slower than that in pure EMA, thus hindering the loss of surfactant molecules in organoclays, resulting in higher thermal stability of organoclay stacks than those dispersed in the EVA matrix.

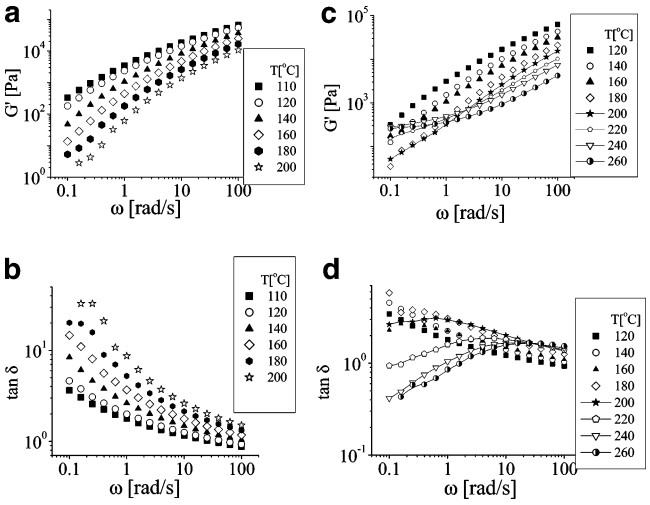

Figure 6. Thermorheological behavior of pure EVA: (a) G' and (b) tan δ, where the meltlike rheology in pure EVA8 (according to Winter's criteria[27]) is seen in all tested temperatures (i.e., rheological responses follow the time−temperature superposition (TTS) principle). Thermorheological behavior of EVA8−C6A (2 wt %) nanocomposite (c) G' and (d) tan δ, where the pseudo-solid rheology in EVA8−C6A (2 wt %) above 160 °C is seen (i.e., deviations from the TTS principle are strongly pronounced at $T > 160$ °C).

The scattering signals in C20A-based nanocomposites are usually much weaker than those in C6A-based systems, which hinder the detailed quantitative analysis of SAXS profiles for C20A-based nanocomposites. Nevertheless, the characteristics of the $d(T)$ dependence for EVA−C20A and EMA−C20A are very similar to their C6A analogues, showing a distinct decrease in the average d-spacing with increasing temperature.

TEM Imaging of Nanocomposite Morphology. TEM observations confirmed the mixed intercalated−exfoliated morphology in the chosen nanocomposite systems. Figure 5 illustrates the typical TEM image in an EVA3−C20A (10 wt %) nanocomposite sample, where both exfoliated and intercalated clay structures are seen. On the basis of TEM observations, we found that exfoliation was more efficient in the system containing C20A organoclay than that in the system containing C6A organoclay. This finding is consistent with our earlier conclusion that higher surfactant content decreases the degree of exfoliation in clays.[7,8]

Rheological Behavior. The dynamic rheological behavior (obtained by oscillatory shear at $\gamma_0 = 0.06$) of tested nanocomposites strongly depends on the concentration of organoclay (ϕ), and results are shown in Figures 6 and 7. It is seen that, in polymer melts (Figures 6,b) or in nanocomposites, when the clay content is low ($\phi \leq 2$ wt %) and temperature does not exceed 180 °C (Figure 6c,d), the slope in tan $\delta(\omega)$ dependence remains negative over the whole range of tested frequencies ($0.1 < \omega < 100$ rad/s), which indicates the meltlike rheological behavior according to Winter's criteria[27] (Table 1). However, as the temperature increases to 200 °C, the shape of tan $\delta(\omega)$ curves changes (Figure 6d). That is, the slope in tan $\delta(\omega)$ at low ω ($0.1 < \omega < 5$ rad/s) becomes positive, indicating the transition from meltlike to solid-like behavior.[27,28] At higher organoclay contents ($\phi = 5$, 10 wt %), EVA and EMA nanocomposites (Figure 7) exhibit pseudo-solid rheology over the whole range of tested temperatures (110−260 °C). For example, above 200 °C in a low-frequency range, the magnitudes of G' and G'' increase with

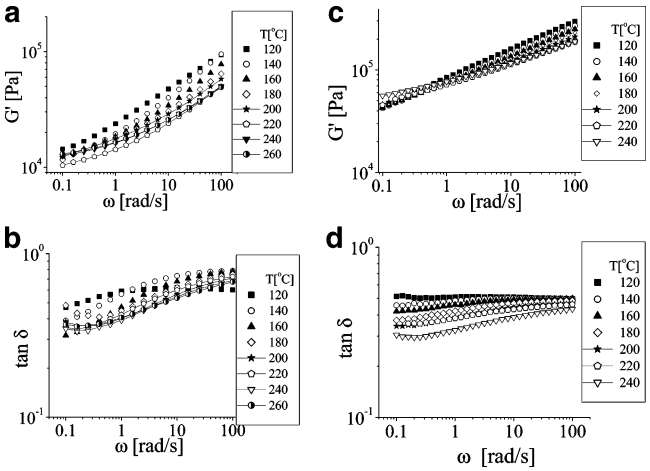

Figure 7. Thermorheological behavior of EVA8−C6A (10 wt %) nanocomposites: (a) G' and (b) tan δ, thermorheological behavior of EMA3−C20A (10 wt %) nanocomposites: (c) G' and (d) tan δ. Pseudo-solid rheological behavior (according to Winter's criteria[28]) is seen in both samples in the whole range of tested temperatures (e.g., deviations from the TTS principle; weak temperature dependence of rheological properties).

Table 1. Thermorheological Behavior of EVA8−C6A Nanocomposites[a]

organoclay concn (wt %)	temperature (°C)							
	120	140	160	180	200	220	240	260
2	m	m	m	g	g	g	g	g
5	m	m	g	g	g	g	g	g
10	g	g	g	g	g	g	g	g

[a] m = meltlike behavior; g = gellike behavior (based on Winter's criteria[28]).

temperature, while the slopes of the $G'(\omega)$ and $G''(\omega)$ dependencies decrease (Figure 7), which is consistent with pseudo-solid rheology. Furthermore, the experimental observations indicate that, in all tested EVA− and EMA−organoclay systems, the pseudo-solid rheological behavior becomes more pronounced upon heating above 180−200 °C.

In Figure 6, it is seen that in the meltlike domain of pure EVA (or EMA) or nanocomposites with low organoclay loading ($\phi \leq 2$ wt %) the tested system follows the time−temperature superposition (TTS) principle. However, materials showing the pseudo-solid rheological behavior greatly deviate from the TTS principle. It can be clearly seen in EVA− and EMA−organoclay nanocomposites that the storage and loss moduli increase with the increase in temperature (Figure 7), indicating the formation of a stronger gel. Deviations from TTS become more pronounced at higher temperatures and higher organoclay contents. In this study, we found that the deviation from the TTS principle was stronger for the C20A-based systems than their C6A analogues, which is consistent with our earlier report.[7,8]

The thermally induced melt-pseudo-solid transition (i.e., gelation) observed in EVA− and EMA−organoclay systems is at least partially reversible. For instance, the EMA3−C6A (2 wt %) nanocomposite could recover the meltlike rheological behavior after cooling from 260 to 120 °C. However, the nanocomposites after the heating/cooling cycle exhibited higher values of G' and G'' and lower values of tan δ than the sample before heating (Figure 8a,b). We hypothesize that the higher stiffness in samples after the heating/cooling cycle may be attributed to the reduced compatibility between the

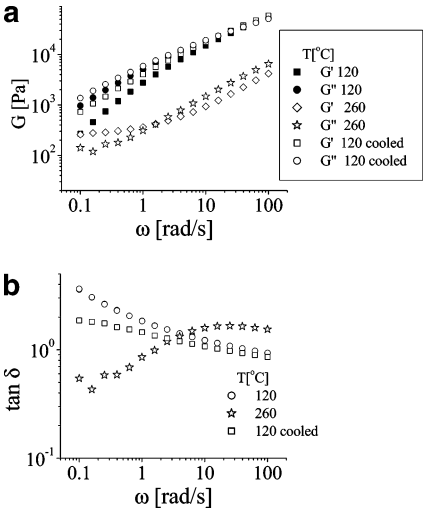

Figure 8. Reversible character of thermally induced physical gelation in EVA8−C6A (2 wt %) nanocomposite: (a) G' and (b) tan δ.

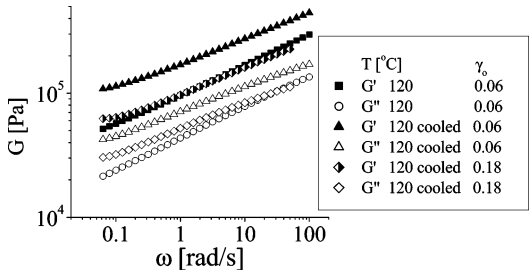

Figure 9. Reversible character of thermally induced physical gelation in EMA3−C20A (10 wt %) nanocomposite in air (EMA3−C20A was first heated to 260 °C and then cooled to 120 °C). The decrease in G' and G'' with the increase in strain amplitude γ_0, which is consistent with the behavior of physical gelation.

organoclay and polymer matrix, caused by the loss of surfactant on organoclay during the heating−cooling cycle.

The observed trends of reversible stiffening at higher temperatures were found to be similar in air and in nitrogen atmospheres, indicating that the behavior of the melt−gel transition can be attributed to the thermally induced aggregation (or deintercalation) of organoclays rather than the chemical cross-linking of a polymer matrix caused by the oxidation and degradation processes. Indeed, for EMA3−C20A nanocomposites heated to 260 °C in air and then cooled to 120 °C, several interesting features were seen (Figure 9). (1) The shapes of rheological curves ($G'(\omega)$ and $G''(\omega)$) predominantly recovered upon cooling. (2) Both G' and G'' significantly increased during the heating−cooling cycle. (3) G' and G'' drastically decreased with the increase in strain amplitude γ_0 over the whole range of tested frequencies. These features are consistent with the rheological behavior of structured fluids (i.e., physical gels or condensed dispersions[29]).

Analysis of Rheological Data (Transition from Modified Cole to LN Behavior). $G'(\omega)$ and $G''(\omega)$ dependencies for tested nanocomposites were fitted using the modified Cole (MC) or log−normal (LN) model in the following form:

$$G^*(\omega) = G_{\text{ind}} + Gg(\omega) \tag{12}$$

where $g(\omega)$ is frequency-dependent modulus expressed

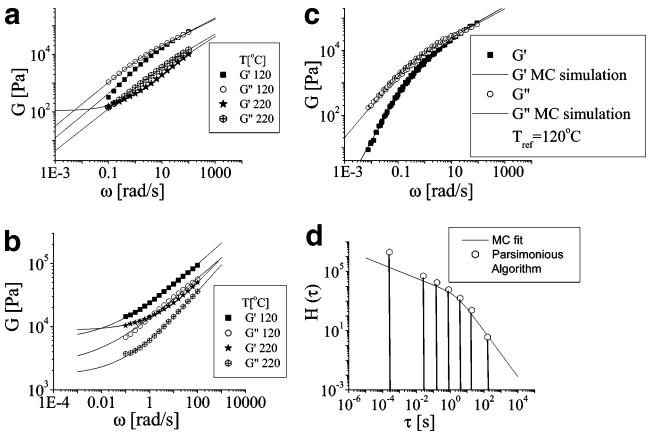

Figure 10. Experimental rheological data vs numerical model fit. (a) Rheological results (symbols) from EVA8−C6A (2 wt %) fitted by the modified Cole (MC) model (lines). (b) Rheological results (symbols) from EVA8−C6A (10 wt %) fitted by the log−normal distribution (LN) model (lines). (c) Fitting of the master curve with $T_{ref} = 120$ °C for EVA8 melt by the MC model. (d) $H(\tau)$ calculated from the data in (c) using Winter's Parsimonious model[12] (open symbols) vs Stieltjes inversion of MC fit[16,17] (solid lines).

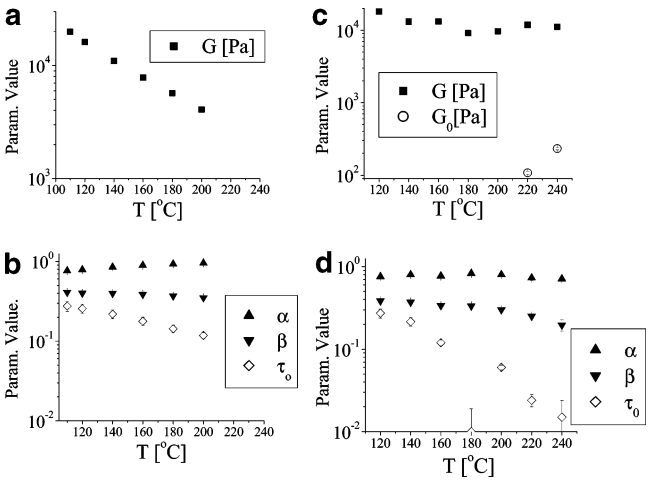

Figure 11. Temperature dependences of rheological parameters using the MC model fit: (a, b) pure EVA8 polymer; (c, d) EVA8−C6A (2 wt %) nanocomposites.

by eq 4 for the MC model or eq 11 for the LN model, and G_{ind} is the frequency-independent component. We found out that, in order to fully describe the experimental data for systems containing high loads of organoclay complex, values of G_{ind} must be used (i.e., $G_{ind} = G_0 + iG_1$).

We suggest that at sufficiently high loading of organoclay a significant fraction of the organoclays are not exfoliated or intercalated by the polymer chains and remain as tactoids. Although the effective aspect ratio of tactoid (say around 10) is not as high as the aspect ratio of individual clay platelet (say around 100), the aggregation of anisotropic tactoids can form an effective 3D network structure within the polymer matrix. The rheological behavior of such a network structure is quite different from that of the pure polymer. Thus, we propose that $g(\omega)$ is dominated by the relaxation modes of polymer, yet reinforced by the clay particles, whereby G_{ind} is characteristic of the tactoid network with G_0 being the elastic modulus and G_1 being the loss modulus due to the disruption of the tactoid network under shear. The notion of a complex character for frequency-independent modulus (G_{ind}) sounds somewhat controversial as it implies the possibility of viscous energy loss in the absence of shear ($\omega \rightarrow 0$). However, we can justify this assignment from the observation of the plateau region in experimental $G''(\omega)$ curves acquired in the nanocomposites with high organoclay loading (Figure 7). Thus, we suggest that while G_1 in nanocomposites must decay to zero when log $\omega \rightarrow -\infty$ ($\omega \rightarrow 0$), its frequency dependence is much weaker than that of pure polymer. As the exact nature of this behavior may not be determined from the available experimental data, we assumed G_1 to be constant in order to avoid overinterpretation. We plan to investigate the character of $G_1(\omega)$ dependence in the future by creep and stress-relaxation measurements, which should reveal more insight into the rheological behavior in a long relaxation time domain.

Results from the quantitative analysis of thermorheological behavior of EVA− and EMA−organoclay systems, as shown in Figure 10, suggest that unusual rheological properties observed in nanocomposites are consistent with thermally induced physical gelation. Indeed, for pure EVA or for nanocomposites of low organoclay loading (i.e., below the gelation threshold as defined by Winter's criteria[27]), the rheological behavior can be satisfactorily described using the MC model (Figure 10a). On the other hand, for the pseudo-solid behavior observed in materials of high organoclay loading, the rheological behavior of nanocomposites may be best described by the LN model, developed for the description of plastic solids[18,19,30] (Figure 10b as well as Table 1).

It is seen that for pure EVA melt (or nanocomposites of low organoclay loading) results from the inversion into a relaxation spectra using the MC model (eq 4) followed by the Stieltjes inversion approach (eq 5) are in surprisingly good agreement with the relaxation time distribution $H(\tau)$ calculated using Winter's parsimonious model[28] (Figure 10c,d), which proves the validity of both approaches for meltlike systems. We found that in pure EVA G_0 is zero for the whole range of tested temperatures. At the same time, the values of G and τ_0 decrease with temperature while the shape parameters α and β do not change much. However, introduction of 2 wt % of C6A organoclay results in a drastic change in the thermorheological behavior (rheological results from EVA8−C6A (2 wt %) nanocomposite are shown in Figure 11). It is seen that the temperature dependence of G in EVA8−C6A (2 wt %) nanocomposite becomes very weak; G_0 becomes positive at 220 °C and increases with temperature (to 240 °C). Moreover, τ_0 is found to decrease with temperature—its decrease is more pronounced than that in pure EVA, while α and β still remain about constant (their values are similar to those in pure EVA8). As the parameters α, β, and a define the shape of distribution of relaxation times $H(\tau)$ rather than the shape of filler particles (e.g., the d spacing change in Figure 4), we suggest that in the described pseudo-solid systems the shape of $H(\tau)$ is predominantly determined by the mechanical/relaxation properties of a filler network rather than by a shape on individual particles or aggregates. Hence, it is feasible that partial aggregation of a filler does not have a strong effect on values of α, β, and a.

The situation drastically changes at higher organoclay loading, where the MC model is no longer suitable to fit the data. This indicates a qualitative change in the asymptotic behavior of the relaxation times distribution

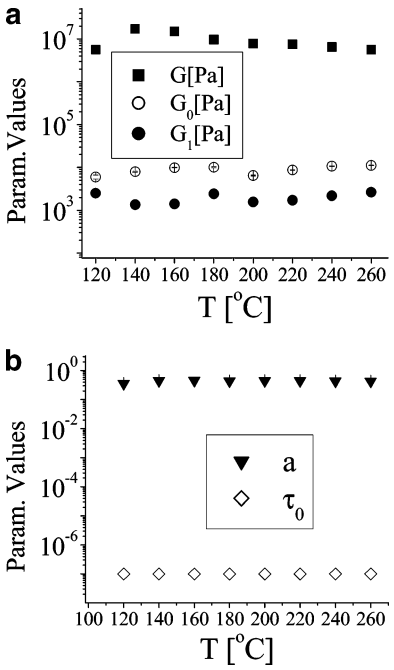

Figure 12. Temperature dependences of rheological parameters using the LN model fit for EVA8−C6A (10 wt %) nanocomposites: (a) G, G_0, and G_1, (b) a and τ_0.

(or at least of its relevant tail toward large relaxation times) from a slowly decaying algebraic power law to a fast exponential decay on the log τ scale. The temperature dependence of parameters from the LN fit is shown in Figure 12. It is seen that the temperature dependences of G, G_0, and G_1 are rather weak (G_0 and G_1 are positive in the whole range of tested temperatures (120−260 °C)), which is consistent with the characteristics of physical gel in EVA8-C6A (10 wt %) nanocomposites. It is interesting to note that G_0 and G_1 vary somewhat as temperature increases from 120 to 200 °C. However, they gradually increase above 200 °C. It is conceivable that thermally induced phase separation results in the aggregation of clay layers and tactoids, causing stiffening of the network structure. At the same time, the polymer matrix becomes softer when temperature increases. The overall effect on rheological behavior is determined by the balance of these opposing factors. In particular, at temperatures above 200 °C, the rheology of nanocomposite is dominated by the segregated network of clay tactoids, while the contribution of the polymer matrix is rather weak. As a result, G, G_0, and G_1 all increase when the degree of clay segregation increases as a result of the surfactant loss in organoclays.

The relationship between MC and LN models may be best demonstrated using the system with intermediate content of organoclay, such as EVA8−C6A (5 wt %) (Figure 13). This nanocomposite is in a gel regime (Table 1), so the quality of the fit is better using the LN model (Figure 13c,d) than the MC model (Figure 13a,b). By comparing the MC and LN fits obtained from the same set of experimental data, it is seen that, while the magnitudes of parameters such as G_0 and τ_0 for the different models cannot be compared directly, the tendencies observed in the character of temperature dependence for these parameters are very similar. For example, G_0 increases with temperature in both models, indicating the formation of stiffer tactoid network, while G decreases due to the softening of the polymer matrix.

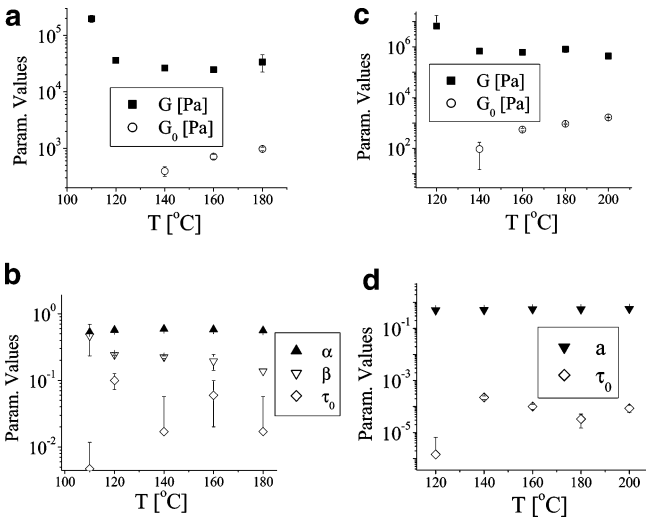

Figure 13. Temperature dependences of rheological parameters for EVA8−C6A (5 wt %) nanocomposite: Relaxation times distribution parameters fitted by the MC model (a) and (b) as well as fitted by the LN model (c) and (d).

Values of the shape parameters (α and β or a) do not change much with temperature for either the LN or MC model. (We note that the τ_0 parameter could not be determined with sufficient precision in both models because of the limited accessible frequency range. As the frequency ($\omega = 2\pi/\tau_0$) lied well beyond the 0.1−100 rad/s range, the error for τ_0 was rather large (>100%) in this study.)

Discussion

It is interesting to note that while the loss of surfactant due to desorption and thermal degradation is insignificant below 170 °C in pure organoclays[10] the average d-spacing for intercalated clay stacks in EVA decreases significantly. Thus, the observed reduction in d-spacing at lower temperatures cannot be completely attributed to the loss of surfactant. We suggest that this behavior is related to the reduced thermodynamic compatibility between the polymer matrix and the organoclay, i.e., the presence of low critical solution temperature (LCST) type phase behavior. In other words, although some EVA and EMA chains can penetrate the stacks of organoclays at lower temperatures, the extent of intercalation decreases with the increase in temperature.

The reduced compatibility between organoclay and polymer matrix in nanocomposites at high temperatures (above 170 °C) can be understood by the following argument. As the degradation/desorption of surfactant molecules from the mineral surface become pronounced, the process would decrease the compatibility between the polymer matrix and the degraded organoclay. It is conceivable that above 200 °C polymer chains are predominantly excluded from organoclay stacks, whereby the phase separation between polymer and organoclay results in the aggregation of clay particles and enhances physical gelation in nanocomposites. Indeed, our data confirmed that lower surfactant content in organoclay results in the formation of stiffer physical gels in both EVA and EMA having a similar organoclay content. For example, the following orders were observed: G'(EVA−C20A) > G'(EVA−C6A); G'(EMA−C20A) > G'(EMA−C6A), suggesting a higher degree of clay aggregation at a lower surfactant content. The irreversible loss of

surfactant during heating above 200 °C may be the major reason for the incomplete recovery of the rheological properties for EVA nanocomposites after the heating−cooling cycle (Figures 8 and 9). On the other hand, we can also argue that as temperature increases, the entropic factors would favor the segregation between polymer chains and bound surfactant molecules in organoclays, whose mobility is severely reduced by being attached to the mineral surface.

The unusual viscoelastic properties observed in EVA− and EMA−organoclay nanocomposites can be explained as follows. At low temperatures, organoclay is compatible with the polymer matrix; thus, the nanocomposites can possess mixed intercalated−exfoliated clays. At low clay content (ϕ), the system exhibits the meltlike rheology, dominated by viscoelastic properties of the polymer matrix. At higher temperatures, the compatibility between organoclay and polymer decreases, which would result in the removal of polymer chains in intercalated and exfoliated clays and form clay tactoids (as seen by the decreasing d-spacing in SAXS). As the viscosity of the EVA or EMA melt tested in this work is rather high even at temperatures above 200 °C, the rate of diffusion for clay platelets is very slow, so the macroscopic aggregation and sedimentation of clay tactoids is unlikely. Therefore, further macroscopic aggregation of clay platelets can result in the formation of a 3-D tactoid network, which exhibits the pseudosolid rheological behavior.

On the basis of results in this study, we suggest that unusual rheological properties observed in EVA− and EMA−organoclay nanocomposites may be expected in the system with good compatibility between organoclay and the matrix at low temperatures, but poor compatibility at high temperatures. Similar systems may include nylon−organoclay nanocomposites. However, the formation of a 3D tactoid network in the nylon-based system may occur at rather high temperatures, where the rheological behavior is predominantly affected by the thermal degradation of organoclay and the polymer matrix.[31] On the other hand, in poorly compatible systems, such as the blend of organoclay with relatively high molecular weight (M_w > 100 kg/mol) polystyrene prepared by melt-mixing, the degree of exfoliation is low, so the amount of clay tactoids may not be sufficient for the formation of a 3D network.[32]

It has become somewhat an axiom among researchers to develop optimal polymer−organoclay nanocomposites with complete exfoliation of clay platelets based on the concept of full compatibility between organoclay and polymer. However, this may be very difficult to achieve because of the poor thermal stability in organoclays,[10] which often leads to the decreased compatibility between polymer and (somewhat degraded) organoclay at high temperatures. Our results indicate that the partially miscible systems can be of practical importance. For example, in EVA− and EMA−organoclay nanocomposites, the lowered compatibility at high temperatures (T > 200 °C) results in increased viscosity and moduli (G' and G'') values. Combined with weak temperature dependence of the rheological properties and low oxygen permeability, these materials exhibited good fire-retardant properties.[21,32,33] On the other hand, the observed phase separation may have an adverse effect on processing of nanocomposites. This is because the commonly used procedure for compounding of organoclays into nanocomposites includes the preparation of a master batch, containing a high load of organoclay (ϕ > 30 wt %) in a lower melting polymer matrix (e.g., low M_w high-density polyethylene, HDPE, treated by maleic anhydride) at low temperatures (<180 °C), which favors the exfoliation of organoclay. However, during further processing, the master batch is often melt-mixed with higher melting thermoplastic polymers, such as isotactic polypropylene (iPP), at temperatures exceeding 250 °C. In that case, thermally induced phase separation between clay and polymer will take place, which can negatively affect the performance of the final product.

Conclusions

Melt-blending of ethylene−vinyl acetate (EVA) and ethylene−methyl acrylate (EMA) copolymers with Cloisite organoclays resulted in nanocomposites with mixed exfoliated and intercalated clays, which exhibited unusual rheological properties. An increase in the organoclay concentration (from 2 to 10 wt %) not only increased the loss and storage moduli but also profoundly changed the character of $G'(\omega)$, $G''(\omega)$, and tan $\delta(\omega)$ dependencies. Similar rheological changes were also seen at temperatures above 200 °C. The pseudo-solid-like rheological behavior in EVA− and EMA−organoclay nanocomposites is related to the physical gelation due to the formation of a 3D tactoid network in the polymer matrix.

The factors controlling the gelation behavior include the overall content of organoclay and the miscibility between organoclay and polymer. The SAXS data indicated that the silicate gallery spacings (d), intercalated by EVA and EMA chains, decreased with increasing temperature. At temperature above 200 °C, the desorption of surfactant in organoclay decreased the compatibility between clay and polymer, which exhibited a LCST-type behavior between organoclays and polymer, enhancing the state of physical gelation. This behavior manifested itself by a reverse temperature dependence of viscoelastic properties (G' is higher at 220 than at 200 °C) and strong deviation of rheological behavior from the time−temperature superposition principle. Nanocomposites with low organoclay loads (e.g., ϕ = 2 wt %) could partially recover the meltlike properties upon cooling, suggesting some reversibility of the clay aggregation process. The rheological behavior of nanocomposites below the gelation threshold could be described by the modified Cole (MC) model, while the rheology of gellike nanocomposites could be described by the log−normal (LN) model. The temperature dependencies of parameters in these rheological models could be correlated with the composition and morphology of the polymer matrix as well as the organoclay content in nanocomposites.

Acknowledgment. This study was supported by a NIST Grant No. 70NANB3D1100, an NSF Inter-American Grant (DMR0302809), an NSF MRSEC (DMR 0080604) at Stony Brook, and a DuPont Aid-in-Education grant. The authors particularly thank R. H. Horst, H. H. Winter (UMASS Amherst), W.-J. Choi (KAIST), A. H. Tsou (ExxonMobil), K. T. Gam, and H. J. Sue (Texas A&M) for their technical assistance and helpful discussions.

References and Notes

(1) Ren, J.; Silva, A. S.; Krishnamoorti, R. *Macromolecules* **2000**, *33*, 3739−3746.

(2) Galgali, G.; Ramesh, C.; Lele, A *Macromolecules* **2001**, *34*, 852−858.
(3) Krishnamoorti, R.; Giannelis, E. P. *Macromolecules* **1997**, *30*, 4097−4102.
(4) Alexandre, M.; Dubois, P. *Mater. Sci. Eng.* **2000**, *28*, 1−63.
(5) Giannelis, E. P.; Krishnamoorti, R.; Manias, E. *Adv. Polym. Sci.* **1999**, *138*, 107−147.
(6) LeBaron, P. C.; Wang, Z.; Pinnavaia, T. *J. Appl. Clay Sci.* **1999**, *15*, 11−29.
(7) Gelfer, M.; Song, H. H.; Liu, L.; Avila-Orta, C.; Yang, L.; Si, M.; Hsiao, B.; Chu, B.; Rafailovich, M.; Tsou, A. H. *Polym. Eng. Sci.* **2002**, *42*, 1841−1851.
(8) Gelfer, M.; Burger, C.; Avila-Orta, C.; Yang, L.; Sics, I.; Hsiao, B. S.; Chu, B.; Si, M.; Rafailovich, M.; Sauer, B. B.; Choi, W.-J.; Kim, S. C. *Proceedings of the International Symposium on Polymer Nanocomposites Science and Technology*, *Oct 2003, Boucherville, Quebec, Canada*; Paper #10.
(9) Cole, K. S.; Cole, R. H. *J. Chem. Phys.* **1941**, *9*, 341−351.
(10) Gelfer, M.; Burger, C.; Fadeev, A.; Sics, I.; Chu, B.; Hsiao, B. S.; Heintz, A.; Kojo, K.; Hsu, S.-L.; Si, M.; Rafailovich, M. *Langmuir* **2004**, *20*, 3746−3758.
(11) Hermans, J. J. *Recl. Trav. Chim. Pays-Bas* **1944**, *63*, 211−234.
(12) Winter, H. H. J. *Non-Newtonian Fluid Mech.* **1997**, *68*, 225−239.
(13) Kohlrausch, F. *Pogg. Ann. Phys.* **1847**, *12*, 393; **1863**, *29*, 337.
(14) Davidson, D. W.; Cole, R. H. *J. Chem. Phys.* **1950**, *18*, 1417−1417; **1951**, *19*, 1484−1490.
(15) Havriliak, S.; Negami, S. *J. Polym. Sci.* **1966**, *C14*, 99−117.
(16) Tschoegl, N. W. *Rheol. Acta* **1971**, *10*, 582−594.
(17) Tschoegl, N. W. *Phenomenological Theory of Linear Viscoelastic Behavior*; Springer-Verlag: New York, 1989.
(18) Drozdov, A. D.; Al-Mula, A.; Drozdov, D. A.; Gupta, R. K. *Los Alamos National Laboratory*, *Preprint Archive*, *Condensed Matter,* 2003; pp 1−33.
(19) Drozdov, A. D.; Christiansen, J. D. C. *Polymer* **2003**, *44*, 1211−1228.
(20) Xie, W.; Gao, Z. M.; Liu, K. L.; Pan, W. P.; Vaia, R.; Hunter, D.; Singh, A. *Thermochim. Acta* **2001**, *367*, 339−350.
(21) Gilman, J. W.; Jackson, C. L.; Morgan, A. B.; Harris, R.; Manias, E.; Giannelis, E. P.; Wuthenow, M.; D. Hilton; Phillips, S. H. *Chem. Mater.* **2000**, *12*, 1866−1873.
(22) Balogh, M.; Laszlo, P. *Organic Chemistry Using Clays*; Springer-Verlag: New York, 1993.
(23) Flory, P. J. *Trans. Faraday Soc.* **1955**, *51*, 848−857.
(24) Kim, M. H.; Phillips, P. J.; Lin, J. S. *J. Polym. Sci., Part B: Polym. Phys.* **2000**, *38*, 154−170.
(25) Richardson, M. J.; Flory, P. J.; Jackson, J. B. *Polymer* **1963**, *4*, 221−237.
(26) Reynolds, R. C. In *Crystal Structures of Clay Minerals and Their X-ray Identification*; Brindley, G. W., Brown, G., Eds.; Mineralogical Society: London, 1980; pp 249−305.
(27) Winter, H. H. *J. Non-Newtonian Fluid Mech.* **1997**, *68*, 225−239.
(28) Winter, H. H.; Mours, M. *Adv. Polym. Sci.* **1997**, *134*, 166−233.
(29) Sim, H. G.; Ahn, K. H.; Lee, S. J. *J. Non-Newtonian Fluid Mech.* **2003**, *112*, 237−250.
(30) Sollich, P. *Phys. Rev. E* **1998**, *58*, 738−759.
(31) Gao, F. In Proceedings of Fourth World Congress on Nanocomposites 2004, San Francisco, Sept 2004, ECM 2004.
(32) Gelfer, M. Y.; Song, H. H.; Liu, L.; Hsiao, B. S.; Chu, B.; Rafailovich, M.; Si, M.; Zaitsev, V. *J. Polym. Sci., Part B: Phys.* **2002**, *41*, 44−54.
(33) Alexandre, M.; Beyer, G.; Henrist, C.; Cloots, R.; Rulmont, A.; Jerome, R.; Dubois, P. *Macromol. Rapid Commun.* **2001**, *22*, 643−646.

MA0475075